Wärme- und Stoffübertragung 21, 233–245 (1987)

Wärme- und Stoffübertragung

Heat and mass transfer in direct contact hygroscopic condensation *

N. Brauner, D. Moalem Maron and **S. Sideman,** Israel

Abstract. A theoretical analysis of direct contact hygroscopic-condensation of cold vapor on hot films is presented. The condensation of the relatively low temperature, low pressure, vapors on a hot film of an hygroscopic brine solution may occur due to the reduced vapor pressure of a sufficiently concentrated solution.

The driving force for condensation is the difference between the partial pressure of water in the brine and the partial pressure of the condensing water vapor. The condensation is also governed by simultaneous mass transfer mechanisms, due to a non-isothermal absorption, with a possible opposing thermal driving force in the condensing vapor phase. The overall performance is determined by the accumulating effects of the various resistances to heat and mass transfer. The present study is aimed to elucidate the controlling mechanisms associated with this absorption-condensation process, and suggest overall transfer rates at the laminar and turbulent flow regimes.

Wärme- und Stofftransport bei hygroskopischer Kondensation unter direktem Kontakt

Zusammenfassung. Es wird eine theoretische Analyse der hygroskopischen Kondensation eines kalten Dampfes auf heißem Film bei unmittelbarem Kontakt vorgestellt. Diese Kondensation bei relativ niedriger Temperatur, niedrigem Druck des Dampfes auf heißem Film einer hygroskopischen Sole-Lösung kann auftreten durch Druckerniedrigung über einer genügend hoch konzentrierten Lösung.

Die treibende Kraft für die Kondensation ist der Unterschied zwischen dem Partialdruck des Wassers in der Sole und dem Partialdruck des kondensierenden Wasserdampfes. Die Kondensation wird auch durch gleichzeitig auftretende Stofftransportmechanismen gesteuert, resultierend aus einer nichtisothermen Absorption, die durch eine entgegengesetzte, thermische treibende Kraft in der kondensierenden Dampfphase ermöglicht wird. Das gesamte Verhalten wird bestimmt durch die akkumulierenden Effekte der verschiedenen Widerstände auf den Wärme- und den Stofftransport. Die vorliegende Studie hat zum Ziel, diese steuernden Mechanismen, die mit Absorptions- und Kondensationsprozessen verbunden sind, zu klären und es wird ein mittlerer Wärmeübergangskoeffizient für laminare und turbulente Strömungsbereiche vorgeschlagen.

Nomenclature

C_b	salt concentration in the brine, kg salt/kg solution
C_b^*	equilibrium salt concentration, kg salt/kg solution
C_{bm}^*	equilibrium salt concentration at temperature T_m and pressure P_{ci}
C_s	interfacial salt concentration $C_s = C_b^*(T_b, P_c)$ kg salt/kg solution
C_w	water concentration in the brine, kg water/kg solution
c_p	specific heat kJ/kg °C
d_c	plate spacing, m
D	diffusion coefficient of salt in the brine, m²/sec
D_H	hydraulic radius for vapor flow, m
F	heat transfer amplification factor due to waviness, Eq. (B.8)
g	gravitational acceleration, m/sec²
h_m	heat transfer coefficient to the wall, kJ/sec m² °C
h_s	interfacial heat transfer coefficient, kJ/sec m² °C
j	enthalpy, kJ/kg
k	thermal conductivity, kJ/sec m °C
K_b	absorption mass transfer coefficient, m/sec
L	required plate length, m
m	local condensation flux, kg/sec m²
M	overall condensation rate, kg/sec m
$Nu_c, \overline{Nu_c}$	nondimensional local and average condensation heat flux, Eqs. (8), (9)
$\overline{Nu_m}$	nondimensional average heat flux through the wall, Eq. (10)
P_c	local vapor pressure, N/m²
Pr	Prandtl number, $c_p \mu/k$
q_m	local heat flux transferred through the wall, kJ/m² sec
q_s	local interfacial heat flux, kJ/m² sec
Q_m	overall heat transferred through the wall, kJ/sec
Q_c	overall heat released during condensation, kJ/sec
Sc	Schmidt number, $\mu/\varrho D$
$Sh_c, \overline{Sh_c}$	nondimensional local and average condensation mass flux, Eqs. (6), (7)
T	temperature, °C
T_{bi}^*	equilibrium brine temperature at initial brine concentration C_{bi}
T_m	wall temperature, °C
u_c	vapor velocity, m/sec
W_c	local vapor mass flow rate (per unit width), kg/sec m
z	downstream distance, m

Greek letters

γ	nondimensional concentration
Γ	mass flow rate (per unit width) kg/sec m
δ	film thickness, m
ΔH_{dil}	heat of dilution, kJ/kg
λ	latent heat of pure water vaporization, kJ/kg
λ^*	latent heat of vaporization of brine, kJ/kg

* Dedicated to Prof. Dr.-Ing. U. Grigull's 75th birthday

λ^*_{ef} effective latent heat of condensation, Eqs. (A.14)–(A.16)
μ viscosity, kg/m sec
ξ nondimensional downstream distance
χ stream quality, kg vapor/kg mixture
ϱ density, kg/m^3
σ surface tension, N/m
θ nondimensional temperature
τ_s interfacial shear stress, N/m^2

Subscripts

b brine film
c condensing vapor
i at inlet
m wall
N Nusselt's solution
o at bottom (outlet)
s interfacial
$*$ at thermodynamic equilibrium

1 Introduction

Film type heat exchangers demonstrate high heat transfer coefficients at low temperature differences [1–2] and are utilized extensively in a variety of industrial equipment such as wetted wall columns, packed columns, rectifiers, evaporators, condensers and heat exchangers. Of particular interest here is the process of hygroscopic condensation of relatively low temperature (low pressure) pure vapors on a hot film of an hygroscopic (salt) solution which occurs due to the reduced vapor pressure of the sufficiently concentrated salt solution [3–4]. The driving force for condensation is the difference between the partial pressure of water in the brine solution and the partial pressure of the condensing (water) vapor. The condensation in this case is also governed by mass transfer mechanisms, due to a non-isothermal absorption, with a possible opposing thermal driving force in the condensing vapor phase. Note that, in the absence of noncondensables in the vapor phase, the primary resistance to mass transfer is the film of the brine.

The problem of isothermal, liquid phase controlled, mass transfer into a liquid film has been extensively studied both experimentally [5–8] and theoretically. Most of those experimental studies have been carried in the turbulent film range ($Re > \sim 1500$), and compared with theoretical studies by utilizing the eddy diffusivity concept [9–10]. These have recently been reviewed [6, 10]. The rate of absorption by a liquid film is significantly increased in the presence of a cocurrent gas flow [5, 7, 11–12].

Relatively few experimental studies have been carried out in the laminar-wavy film region, where the waves intensify the transfer rates compared to the expected values for smooth film flow. This enhancement is believed to be due to the convective motion induced by the well-developing rolling waves [13–16].

As the hygroscopic condensation process involves simultaneous heat and mass transfer, the overall performance is determined by the accumulating effects of the thermal resistance of the brine film, and the in series resistance to mass transfer in the brine film, due to the dilution caused by the condensation at the free interface of the brine film.

Yih and Seagrave [17] accounted for the effect of temperature variation across a laminar falling film on the physical properties of the liquid. Nakorayakov and Grigoreva [18, 19] included temperature variation of the film in the flow direction and calculated the shape of the temperature profile across the liquid film, assuming a uniform velocity profile. Grossman [20] improved their models by accounting for the velocity distribution within the liquid film in the laminar and turbulent regions. However, the assumptions incorporated in the solution of the energy and diffusion equations (constant physical properties of the liquid solution, constant flow rate and film thickness, neglect of the interfacial heat transfer and pressure drop in the vapor phase, a constant wall temperature which equals that of the entering liquid film) are insufficient to simulate the practical hygroscopic condensation processes.

The present study is aimed at elucidating the mechanisms associated with the operation of an absorption-condensation unit at various operation conditions.

2 The physical model

A schematic description of a typical hygroscopic-condensation unit of length L is given in Fig. 1. The brine enters with a concentration C_{bi}, temperature T_{bi} and a mass flow rate Γ_{bi}. It falls on vertical parallel surfaces separated by a lateral spacing, d_c. Steam enters the top of the condensation compartment ($Z = 0$) and flows cocurrently to the liquid films. The entering steam has a water vapor pressure, P_{ci} (usually saturated, with a given quality, χ). The saturation temperature, T_{ci} (corresponding to P_{ci}), may be lower than the brine temperature, T_{bi}. However, the relatively cold vapor may be absorbed and condensed by the brine film, providing the brine vapor pressure, P^*_{bi}, is lower than the partial pressure of steam in the condensation compartment, P_c, i.e., $P_c \cong P^*_b(T_{bi}, C_{bi})$. In the absence of noncondensables, the resistance to absorption in the vapor phase is negligible, and a liquid phase controlled condensation-absorption is to be considered, whereby a concentration profile within the liquid film is built-up. The interfacial salt concentration, C_s, is to be determined from the pressure equilibrium condition:

$$P^*_b(C_s, T_b) = P_c \tag{1}$$

or

$$C_s = C^*_b(P_c, T_b) \tag{2}$$

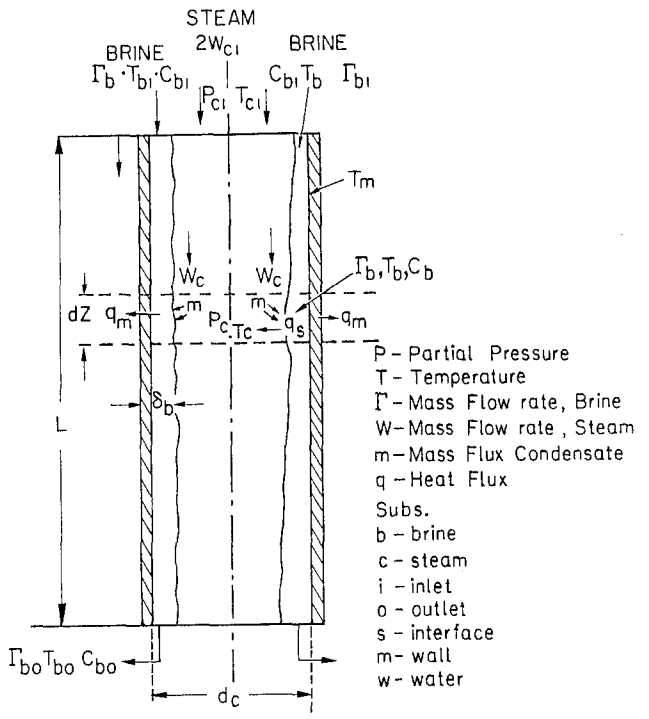

Fig. 1. Schematic description of an hygroscopic condensation compartment of length L

where C_b^* is the thermodynamic equilibrium salt concentration at local conditions of (uniform) temperature T_b and vapor pressure P_c.

The water vapor absorbed at the liquid free interface diffuses into the brine film. The heat generated in the absorption-condensation process results in a simultaneous heat transfer process.

3 The calculation procedures

The mass energy and momentum balances at the interfaces of the condensing vapor and brine as well as the relevant transport coefficients are given elsewhere [27] and are summarized in Appendix A and B.

For a given set of operating variables Γ_{ci}, W_{ci}, T_{bi}, C_{bi}, T_{ci}, χ or (T_{ci}, P_{ci}) specified at $Z=0$, the differential mass, momentum and energy balances on both phases are integrated simultaneously in the downstream direction, utilizing a modified Runge-Kutta procedure. At each integration step the physical properties of the brine film are determined as function of the local temperature T_b and concentration C_b, and the transfer coefficients K_b, h_m, h_s evaluated at the local brine and vapor Reynolds number.

The integration is terminated whenever one of the following conditions is reached:

a) The total rate of vapor absorbed by the brine film equals the vapor input rate, W_{ci}.

b) Zero driving force condition for vapor absorption are reached, namely the local bulk brine concentration C_b equals the local interfacial brine concentration C_s, at the local temperature and pressure conditions, $C_b = C_s^*(P_c, T_b)$.

4 Results and discussion

The operational parameters studied are vapor and brine feed flow rates (W_{ci}, Γ_{bi}), length of the transfer area (L), wall temperature, (T_m), temperature and pressure level of condensing vapor (T_{ci}, P_{ci}) and temperature level of absorbing brine (T_{bi}).

The case chosen for the various demonstrations is 40% (wt) $CaCl_2$ brine ($C_{bi}=0.4$), a flow rate which corresponds to $Re_{bi}=200$, and an operation temperature level $T_m = T_{bi} = 70\,^\circ C$. These conditions correspond to $Sc_{bi}=1070$ and $Pr_{bi}=13.1$. The following nondimensional concentration and temperature are utilized:

$$\theta = \frac{T - T_m}{T_{bi}^* - T_m} \tag{3}$$

$$\gamma_b = \frac{C_{bi} - C_b}{C_{bi} - C_{bm}^*}, \quad \gamma_s = \frac{C_{bi} - C_s}{C_{bi} - C_{bm}^*} \tag{4}$$

where C_{bm}^* is the concentration of a brine at temperature T_m in equilibrium with its vapor at pressure P_{ci}, and T_{bi}^* is the temperature of a solution at concentration C_{bi} in equilibrium with its vapor at pressure P_{ci}. Note that C_{bm}^* is the minimum brine concentration that would be achieved on infinite transferring surface, with the brine temperature approaching the wall temperature and in case no pressure losses exist in the vapor phase. C_{bm}^* may be utilized in Eq. (A.9) to evaluate the maximum absorption potential of the brine film. Substituting $C_{bo} = C_{bm}^*$ in Eq. (A.9) yields:

$$M_{\max} = (\Gamma_{bo})_{\max} - \Gamma_{bi} = \Gamma_{bi}\left[\frac{C_{bi} - C_{bm}^*}{C_{bm}^*}\right]. \tag{5}$$

The equilibrium temperature T_{bi}^* includes the boiling point elevation of a salt solution at concentration C_{bi} in equilibrium with its vapor at pressure P_{ci}. In fact, $T_{bi}^* - T_m$ is a measure of the temperature driving force in the hygroscopic condensation process, instead of $T_c - T_m$ (the latter may even be negative and still condensation takes place).

4.1 Condensation of stagnant vapor, $Re_c = 0$

The limiting case of hygroscopic-condensation of stagnant vapor at constant pressure P_{ci} and temperature T_{ci}, is of particular interest. This corresponds to a case where the spacing between the adjacent transferring plates is increased, so that $Re_c \to 0$. In this case the feed flow rate of the vapor has no effect on the process.

Figure 2a, b present the typical variation of the brine temperature θ_b, and the concentrations γ_b, γ_s with the non-

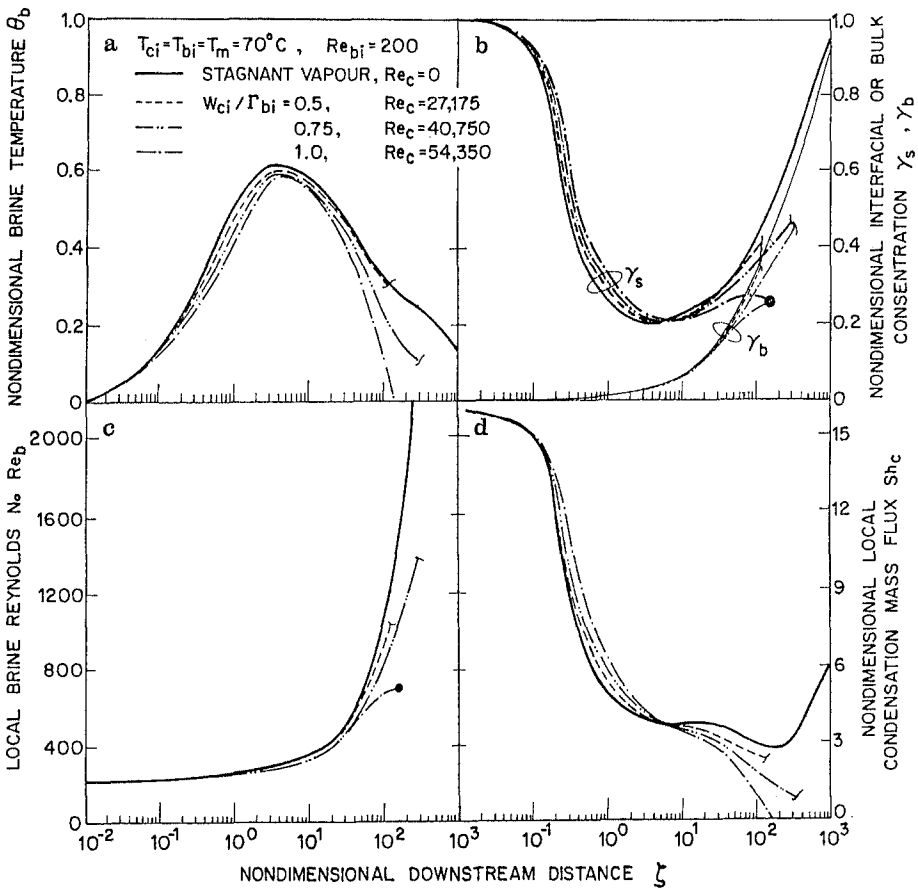

Fig. 2. Absorption characteristics along the plate for various vapor flow rates

dimensional downstream distance, $\xi = z/(\delta_{bi} Re_{bi})$. $Re_c = 0$ is denoted by the solid line. Initially, for small ξ, the brine temperature increases as part of the heat released during the hygroscopic condensation is heating up the brine film. Then, for a sufficiently long transfer surface, the brine temperature approaches the wall temperature, and θ_b decreases, approaching zero ($T_{bi} = T_m$) as the heat is removed through the wall.

The interfacial brine concentration, $C_s = C_b^*(T_b, P_c)$, follows the variation in the brine temperature. Higher brine temperature affects higher concentration and γ_s decreases correspondingly, so that γ_s is in the opposite trend to that of the interfacial temperature. Clearly, the bulk concentration of the brine decreases (γ_b increases) towards the asymptotic value $C_{bm}^* = C_b^*(T_m, P_c)$.

The observed trends for the variation of the brine temperature and concentration are in qualitative agreement with those predicted by Grossman [20], except at the entry region, where the heat and mass boundary layers are build-up. This relatively short entry region has not been considered here since the practical entry region is small relative to the entire transfer length.

In the case studied here where $T_{ci} = T_{bi} = T_m$, no pressure losses exist in the vapor phase, ($P_c = P_{ci}$) and $C_{bm}^* = 0$, the absorption potential of the brine film is, in fact, unlimited ($M_{max} \to \infty$). Consequently, the local brine flow rate increases significantly in the downstream direction. The local brine Reynolds number increases significantly both due to the increase of the local flow rate as well as the marked decrease of a diluted brine viscosity, Fig. 2c.

The local and average nondimensional condensation mass fluxes at the interface are defined by:

$$Sh_c = \frac{m\,\delta_{bi}}{\varrho_{bi}\, D_i (C_{bi}^* - C_{bi})} \tag{6}$$

$$\overline{Sh_c} = \frac{M\,\delta_{bi}}{L\,\delta_{bi}\, D_i (C_{bi}^* - C_{bi})}\,. \tag{7}$$

As indicated in Fig. 2d the local (and average) condensation mass fluxes decreases in the downstream direction, due to the decrease of the hygroscopic condensation driving force ($\gamma_s - \gamma_b$). Far downstream, the moderate decrease in the local driving force is compensated by the increase in the local transfer coefficients due to the increasing local brine Reynolds number, well into turbulent flow regime. Similar trends are observed in Fig. 3a for the nondimensional local (and average) interfacial heat fluxes due to condensation, defined by

$$Nu_c = \frac{q_c\,\delta_{bi}}{k_{bi}(T_{bi}^* - T_m)} \tag{8}$$

$$\overline{Nu_c} = \frac{Q_c\,\delta_{bi}}{L\,k_{bi}(T_{bi}^* - T_m)} \tag{9}$$

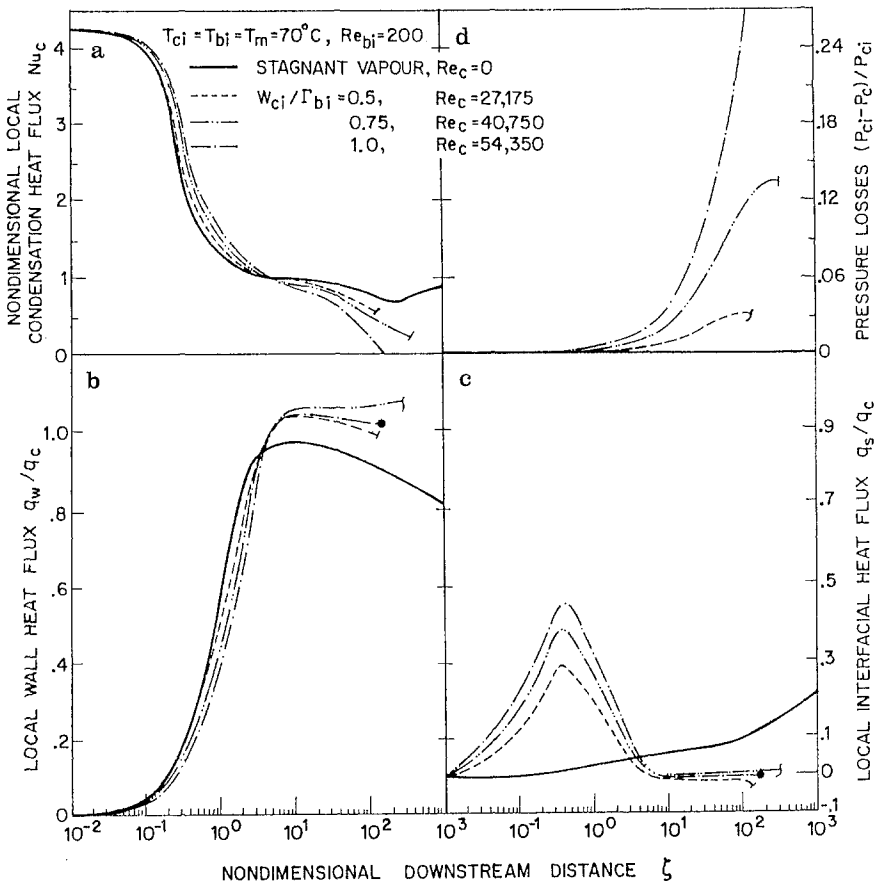

Fig. 3. Heat transfer characteristics and pressure drop for various vapor flow rates

which follow the trends observed for the interfacial mass fluxes. q_c is the local condensation heat flux and Q_c is the overall heat released during condensation.

Part of the heat released during the hygroscopic condensation may be locally used up to heat up the brine film. The rest is removed through the solid wall q_m and through the free interface of the brine to the adjacent vapor phase, q_s. The local ratios q_m/q_c and q_s/q_c are presented in Figs. 3b and 3c. Initially both q_m/q_c and q_s/q_c are low for very small ξ, as most of the heat released during the condensation is used up in heating the brine film (Fig. 2a). As the brine temperature increases, the major part of q_c is transferred through the solid wall and the ratio q_m/q_c approaches unity. Far downstream, q_m/q_c decreases, following the decline of the brine temperature. This is partly compensated by the increased local heat transfer coefficient due to the increasing brine Reynolds number. The heat lost to the adjacent stagnant vapor phase (at constant temperature $T_c=T_{ci}=T^*(P_{ci})$) is relatively small. The heat losses increase moderately in the downstream direction due to the increase of the interfacial heat transfer coefficient with increasing the local brine Reynolds number.

The rate of heat transferred through the solid wall is of particular interest, as it is the rate of heat available for further use outside the system. An average nondimensional heat flux through the wall is defined here by:

$$\overline{Nu_m}=\frac{Q_m\,\delta_{bi}}{L\,k_{bi}(T^*_{bi}-T_m)}. \tag{10}$$

Note that $\overline{Nu_m}<\overline{Nu_c}$ and $\overline{Nu_m}\to\overline{Nu_c}$ for a sufficiently long surface.

4.2 *Effect of vapor flow rate, W_{ci}*

The discussion so far has been limited to hygroscopic-condensation with $Re_c\to 0$. However, for a finite spacing between the transferring plates (here $d_c=2$ cm or $D_H=4$ cm), $Re_c\neq 0$ and the pressure losses in the vapor phase are to be considerd. This is due to the high sensitivity of the local equilibrium interfacial salt concentration $C_s=C^*_b$ to variation of the vapor pressure. Clearly the pressure losses are related to the local vapor flow rate, and thus the rate of vapor entering the condensation compartment affects the condensation process.

As is shown in Figs. 2 and 3, the lines for low vapor feed flow rate ($W_{ci}=0.5\,\Gamma_{bi}$ and $Re_{ci}=27{,}175$) closely follow the characteristics observed for $Re_c\to 0$ and a relatively short transfer surface is required to complete the vapor condensation. However, the vapor temperature is no longer constant and follows the variation of the brine temperature in the downstream direction as heat is ex-

changed between vapor and brine through the free interface. Initially, for small ξ the increase of Re_c affects an enhancement of the interfacial heat flux (Fig. 3c). However, further downstream, the vapor temperature approaches the brine temperature and the interfacial heat flux diminishes.

As the vapor feed flow rate is increased ($W_{ci} = 0.75\,\Gamma_{bo}$, in Figs. 2 and 3), the pressure losses in the vapor phase (Fig. 3d) increase, and the required transfer area increases, affecting lower local downstream pressures. Consequently, the local interfacial brine concentration increases and both the local driving force and the brine absorption potential decrease. With a further increase of the vapor flow rate ($W_{ci} = \Gamma_{bo}$), higher upstream pressure losses further reduce the brine absorption potential, and a point is reached where the local equilibrium salt concentration $C_s = C_b^*(T_b, P_c)$ equals the local brine bulk concentration. The absorption driving force drops to zero (Fig. 2b, d), with the total condensation rate now being less than W_{ci}. In this case the unit is incapable of handling the rate of vapor fed to the system. This phenomenon is further demonstrated in Fig. 4a, where the fraction of vapor condensed M/W_{ci} and the required transfer length are presented as a function of the vapor feed flow rate, W_{ci}/Γ_{bi} (note that Γ_{bi} is constant here, at $Re_{bi} = 200$).

As seen in Fig. 4, increasing the vapor feed flow rate up to $W_{ci}/\Gamma_{bi} \approx 0.8$ results in a total condensation of the vapor ($M/W_{ci} = 1$), provided that the length of the transfer area is correspondingly increased. However, the driving force for absorption significantly diminishes due to the increased pressure losses associated with the higher vapor flow rates and the longer (required) surface. Eventually, one may reach a point, at a certain vapor feed rate, where an asymptotic infinite transfer area is required to accomplish the total condensation rate $M = W_{ci}$. In fact, if the vapor feed rate is now further increased, the transfer area fails to accomplish the total condensation of the incoming vapor feed rate, since the absorption driving force $C_b - C_b^*(P_c, T_c)$ now drops to zero at a certain, finite, length of the transfer area and the condensation fraction as well as the transfer area decrease. It is thus noted that the left side of the transfer length curve (A–B) in Fig. 4a represents the calculated transfer area required for complete condensation. The right side of the transfer length curve (B–C) represents the region wherein increasing the vapor feed rate results in a sharp decrease in the driving force (hence, the absorption rate) due to pressure losses and temperature and concentration changes of the brine. The points on the (B–C) curve thus denote the effective length of the transfer area where $C_b - C_b^*(P_c, T_c) \neq 0$.

The analysis thus indicates that for a given transfer length L, the system may operate either in the low vapor feed rate change, where total condensation of the feed occurs ($M \equiv M_1$) or at the high feed rate range where only partial condensation occurs ($M \equiv M_2 < W_{ci}$). Note that

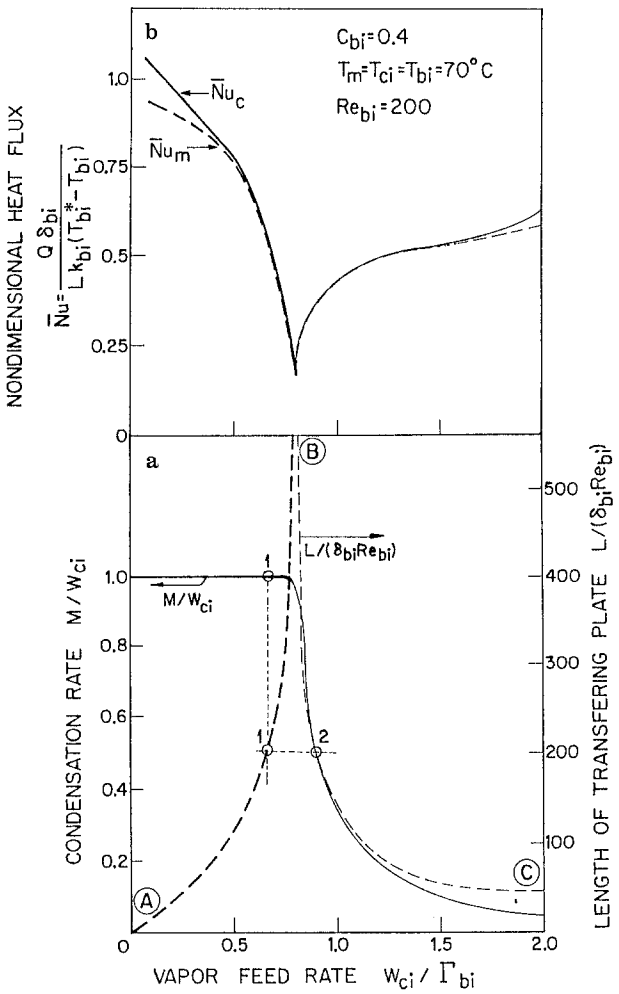

Fig. 4. Effect of vapor flow rate on the overall absorption and heat transfer rates

$M_2 < M_1$. Consequently, when operating at point 2 on Fig. 4a ($M < W_{ci}$), the removal of the unabsorbed vapor is required (by a vaccum pump, for instance). If the remainder uncondensed vapor is not continuously removed from the compartment, the system will in fact stabilize at point 1 at a lower W_{ci} which equals the condensation rate on the given transfer area. In other words, point 2 may represent an unstable operating condition where high vapor rate (W_{ci}) is sucked into the compartment due to momentary low pressure at the exit. However, as vapor accumulates, due to incomplete condensation, the pressure rises and the feed rate decreases until $(W_{ci})_1 = M_1$. Consequently, the region where $M/W_{ci} = 1$ seems to represent a range of stable operation at a specified operating condition, with a maximum condensation potential of about $M = W_{ci} = 0.8\,\Gamma_{bi}$ on an infinite transfer surface. Note that this maximum value is far below the maximum M_{max} predicted by Eq. (5), where the vapor pressure losses were neglected. Complementing Fig. 4a is a presentation in Fig. 4b of the nondimensional condensation heat flux, $\overline{Nu}_c$, and the heat recovered through the wall $\overline{Nu}_m$. As seen

in Fig. 4b, increasing the vapor feed rate in the stable operation range (curve A–B of Fig. 4a), decreases $\overline{Nu_c}$ and $\overline{Nu_m}$, corresponding to the steep increase in the required transfer length and the associated decrease of the average driving force in the process. The average rate of heat recovery through the wall is practically equal to the average rate of heat released during vapor condensation (except at the very low vapor rates), where the condensation is accomplished on a fraction of the surface, and the brine film leaves at relatively high temperature.

Relating now to the 'unstable' range of Fig. 4a, it is seen that the average heat fluxes are recovered with increasing the vapor rate. This is in accordance with the decrease of the effective transfer area observed in this region, and the shorter transfer surfaces associated with higher average driving force.

4.3 *Effect of brine Reynolds number, Re_{bi}*

The effect of the brine Reynolds number, Re_{bi} on the process characteristics is studied here by keeping a constant vapor feed rate (constant Re_{ci}). The selected value of W_{ci} corresponds to the maximum absorption rate observed, i.e., $Re_{bi} = 200$; $W_{ci} = 0.8\,\Gamma_{bi} = 1.25$ gr/cm sec.

As is indicated elsewhere [27] increasing the brine Reynolds number results in an increase of the local and average condensation mass and heat fluxes and the average heat flux recovered through the wall. This is due to the enhanced transfer coefficients associated with increasing Re_{bi}. The increased amounts of heat released during the hygroscopic condensation affects higher brine temperature at the same downstream location. The pressure losses also increase with increasing Re_{bi}. Consequently, the interfacial salt concentration increases (γ_s decrease) leading to a decrease in the condensation driving force, $\gamma_s - \gamma_b$. Thus, the interaction between the momentum, heat and mass transfer tends to moderate the transfer rate enhancement due to increased brine Reynolds number.

The enhanced transfer rates with increasing Re_{bi} affects complete condensation of the vapor on shorter surfaces. This is demonstrated in Fig. 5a, where the fraction of condensed vapor M/W_{ci} and the required transfer length L are presented as functions of Re_{bi}. For $Re_{bi} = 200$, the complete condensation of the incoming vapor ($M = W_{ci}$) is to be accomplished on a practically infinite transfer surface, with the driving force approaching zero downstream. As Re_{bi} increases, the transfer rates improve and although the local pressure losses increase, the required transfer length decreases.

The average condensation heat flux and the average heat flux recovered through the wall (Fig. 5b) increase simultaneously. On the other hand, reducing the brine Reynolds number below $Re_{bi} = 200$ results in incomplete vapor condensation and unstable operation, as discussed with reference to Fig. 4.

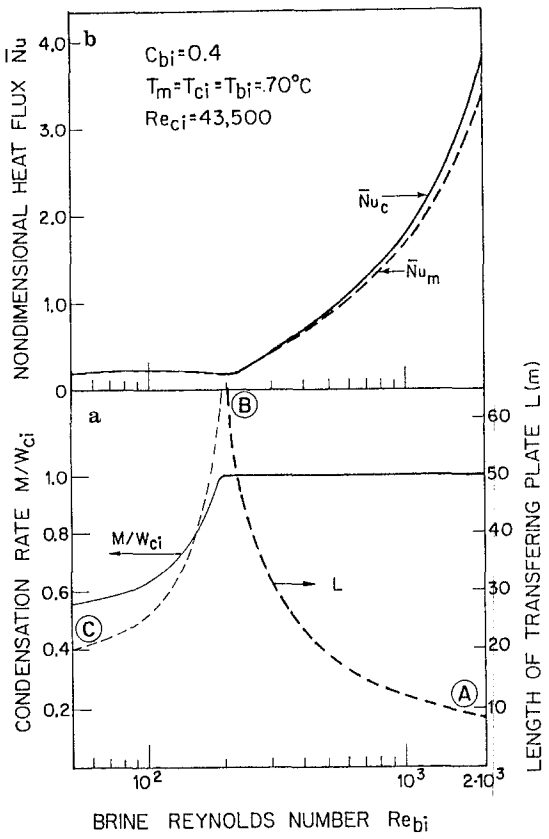

Fig. 5. Effect of brine Reynolds number on the overall absorption and heat transfer rates

4.4 *Effect of the wall temperature*

The effect of the wall temperature T_m on the process characteristics is demonstrated in Fig. 6. Generally, reducing the wall temperature improves the hygroscopic condensation rates and vice versa. Lower wall temperature affects lower brine temperatures (Fig. 6a), as the removal of heat released during the hygroscopic condensation is improved, Fig. 6d. The equilibrium salt concentration at the free interface is reduced accordingly, resulting in a higher driving force which, in turn, enhances the rate of vapor absorption (Figs. 6b and 6c). Consequently, the brine absorption potential increases and the required transfer area decreases.

Increasing the wall temperature above the feed brine temperature, $T_m > T_{bi}$, is of particular interest. As expected, for small downstream distances the brine film is heated up by the heat transferred through the hot wall and by the heat released during the hygroscopic condensation. However, as ξ increases, the brine temperature exceeds the wall temperature and heat is removed from the system through the wall (Fig. 6d). Thus, although the apparent nominal thermal driving force ($T_b - T_m$) implies that heat is transferred from the wall to the brine, the net effect is that heat is transferred from the brine to the wall and $\overline{Nu_m} > 0$.

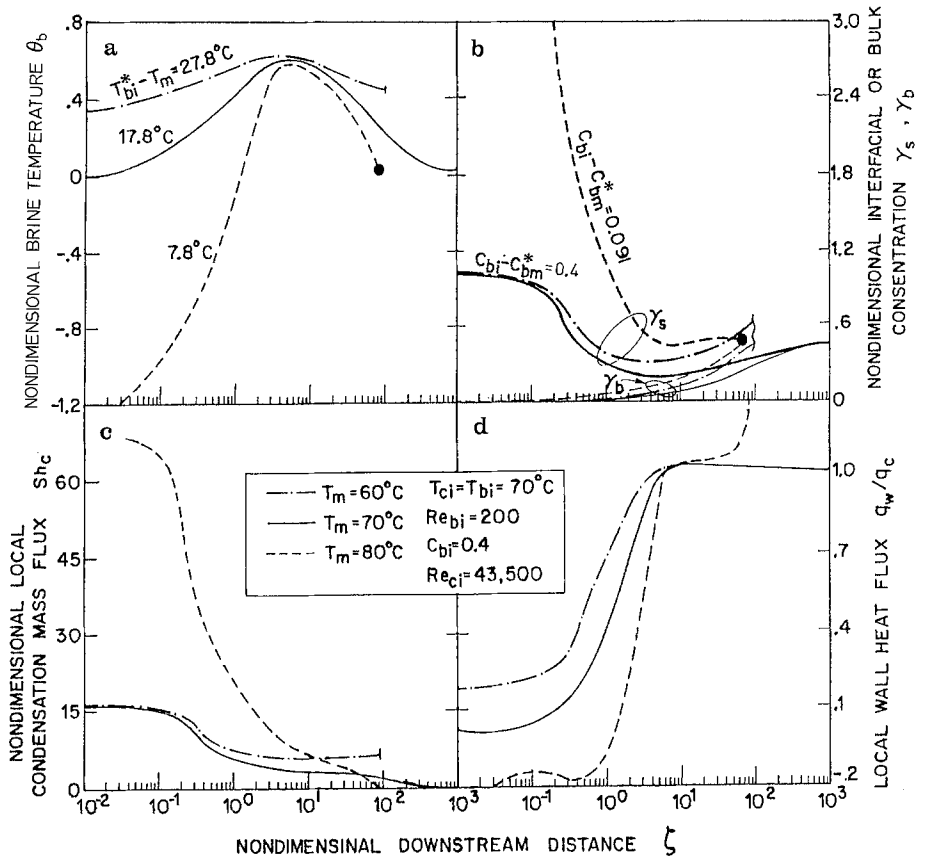

Fig. 6. Various process characteristics along the plate. Effect of wall temperature

The effect of the wall temperature on the overall process performances is demonstrated in Fig. 7. Starting with $T_m = T_{bi} = 70\,°C$ ($\theta_m = 1$), a practically infinite transferring length is required for complete condensation at the specified vapor rate, $M = W_{ci}$. Lower wall temperatures ($\theta_m > 1$) shows complete vapor condensation on a shorter surface (Fig. 7a), with increased average heat fluxes and $\overline{Nu_c} = \overline{Nu_m}$ (Fig. 7b). Therefore, higher vapor rates may be condensed (on longer surfaces) with decreasing the wall temperature for $\theta_m > 1$. At $\theta_m < 1$, the transfer surface fails to condense the vapor feed as a zero driving force ($C_s = C^*_b(T_c, P_c) = C_b$) is reached at a finite downstream distance. Clearly a complete vapor condensation may be achieved at lower rates, when the rate of vapor feed to the condensation compartment is reduced accordingly. In this case the location of the maximum required transferring area and the corresponding minimum average heat fluxes ($\overline{Nu_c}, \overline{Nu_m}$) will be shifted to the left, towards higher wall temperature. However, the condensation rate can never exceed the maximum absorption potential predicted by Eq. (5), for the limit case of $Re_c \to 0$. For $T_m \leqq T_{ci} = T^*(P_{ci})$, $C^*_{bm} \to 0$ and $M_{max} \to \infty$. With $T_m > T_{ci}$, C^*_{bm} increases and a finite limiting absorption potential is obtained. This limiting value is also indicated on Fig. 7a. When the wall temperature is raised to T^*_{bi} then $C^*_{bm} = C_{bi}$ and $M_{max} = 0$, i.e., the hygroscopic condensation process ends.

4.5 Effect of the inlet vapor temperature, T_{ci}

The discussion so far was limited to the case where the inlet vapor was saturated at a temperature $T_{ci} = T_{bi}$ (zero thermal driving force for condensation).

The effect of reducing the temperature level, and the corresponding saturation pressure level $P_{ci} = P^*(T_{ci})$, of the inlet vapor is demonstrated in Fig. 8. A lower inlet pressure P_{ci} affects an increase of the equilibrium salt concentration at the brine free interface $C_s = C^*_b(P_c, T_b)$ and thus the driving force ($C_b - C^*_b$) as well as the limiting brine absorption potential, decrease (C^*_{bm} increase). Note that the nondimensional interfacial salt concentration γ_s increases with reducing P_{ci} (Fig. 8a), which indicates that the reduction in the local driving force is less than might be expected by the reduction of the nominal driving force ($C_{bi} - C^*_{bm}$). The compensation is due to lower brine temperature level (see Fig. 8b), affected by both the enhanced heat transfer to the adjacent, relatively cold, vapor phase and the reduced rate of heat released during the hygroscopic condensation. As is indicated in Fig. 8c, the local condensation heat flux follows the trends observed for the local absorption driving force (Fig. 8a) with the reduction, for lower T_{ci}, being less than might be expected by the reduction of the nominal temperature driving force ($T^*_{bi} - T_m$). These observations manifest the mutual effects of the simultaneous mass and heat transfer process occurring during the hygroscopic condensation.

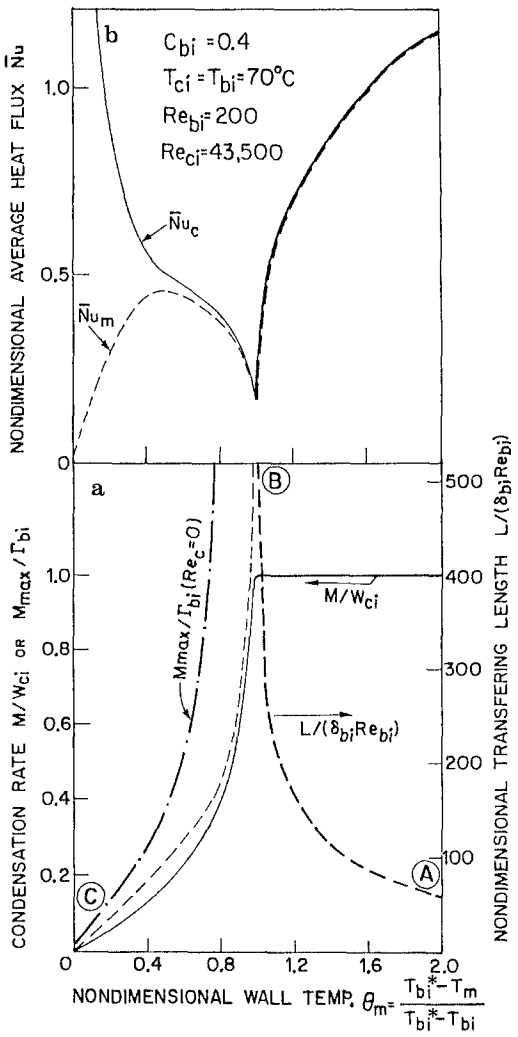

Fig. 7. Effect of wall temperature on the overall absorption and heat transfer rates

The effect of reducing the temperature level of the saturated vapor on the overall unit performance is summarized in Fig. 9. The fraction of vapor condensed M/W_{ci}, the required transferring length and the average heat fluxes, $\overline{Nu_c}$, $\overline{Nu_m}$ are presented as a function of the nondimensional inlet vapor temperature, $\theta_{ci}(\equiv(T_{bi}-T_{ci})/(T_{bi}^*-T_{ci}))$. Note that $(T_{bi}^*-T_{ci})$ express the boiling point rise (BPR) of the brine of concentration C_{bi} at a pressure level P_{ci}. The BPR is insensitive to variations in the pressure level, and for the 40% $CaCl_2$ solution BPR $\cong 17\,°C$.

If the rate of vapor feed equals the maximum absorption potential at $T_{ci}=70\,°C$, reducing T_{ci} from 70 °C leads to an incomplete inlet vapor condensation with a zero driving force reached on at a certain downstream location (see also Fig. 8). The average heat flux recovered through the solid wall $\overline{Nu_m}$ at this temperature range is less than the average condensation heat flux, $\overline{Nu_c}$. For sufficiently low T_{ci}, $\overline{Nu_m}$ reaches negative values, which indicates that heat is transferred from the wall to the brine film which is cooled by the adjacent low temperature vapor phase.

The limiting, maximum, brine absorption potential (Eq. (5)) corresponding to T_{ci} is also included in Fig. 9a. This limiting value of M_{max}/Γ_{bi} as $Re_c \to 0$ (zero pressure losses) corresponds to an infinite transfer length, with $T_b \to T_m$. Clearly, the practical maximum absorption potential which may be achieved in case $Re_c > 0$ (finite pressure losses) and a finite transfer length, with $T_b > T_m$, is less than M_{max}. Consequently, the location of the limit of $M/W_{ci}=1$ for each specified W_{ci}/Γ_{bi} (and the maximum of the required transfer length) lies always to the right (higher T_{ci}) of the curve of M_{max}/Γ_{bi}. Thus, as the inlet vapor temperature is decreased (increasing θ_{ci}), both the practical and limiting maximum brine absorption potential decrease. When $\theta_{ci} \to 1$, the inlet vapors are colder than the brine by an amount which equals the brine BPR, and no condensation of vapor may take place.

4.6 *Effect of process temperature level*

The effect of the process temperature level is obviously of interest. Reducing the temperature level $(T_{bi}=T_{ci}=T_m)$ adversely affects the hygroscopic condensation rate (and vice versa) for the following reasons:

a) Higher brine viscosity, and thus higher brine feed flow rate (affect a thicker film) is required to maintain a constant film Reynolds number.

b) The thermal resistance of the thicker brine film increases, and the rate of heat removal is significantly decreased.

c) Higher vapor velocity, at a desired vapor mass flow rate W_{ci}, due to the decrease of vapor density associated with a lower saturation temperature level. Consequently the pressure losses in the condensation compartment increase.

d) The absorption rates decline due to lower mass transfer coefficient since $K_b \propto D^{1/2}$ and coefficient D decreases significantly with the decreased brine temperature.

The above trends are demonstrated in Fig. 10 where the process characteristics are presented for temperature levels of 50 °C, 70 °C and 75 °C. Note that the nominal concentration driving force $(C_{bi}-C_{bm}^*)$ and the nominal temperature driving force are practically unaffected by the temperature level since the vapor enters at saturation and C_b^* is zero. Reducing the process temperature level from 70 °C and 50 °C results in higher pressure losses (Fig. 10a) and a zero concentration driving force condition is reached downstream (Fig. 10b, c). Consequently, although Γ_{bi} increases, M decreases, and the brine absorption potential (M/Γ_{bi}) is significantly deteriorated (Fig. 10d). On the other hand, increasing the process temperature level $(T_{bi}=T_{ci}=T_m=75\,°C)$ results in a complete condensation of $(M=W_{ci})$ on a shorter transfer length with an additional brine absorption potential.

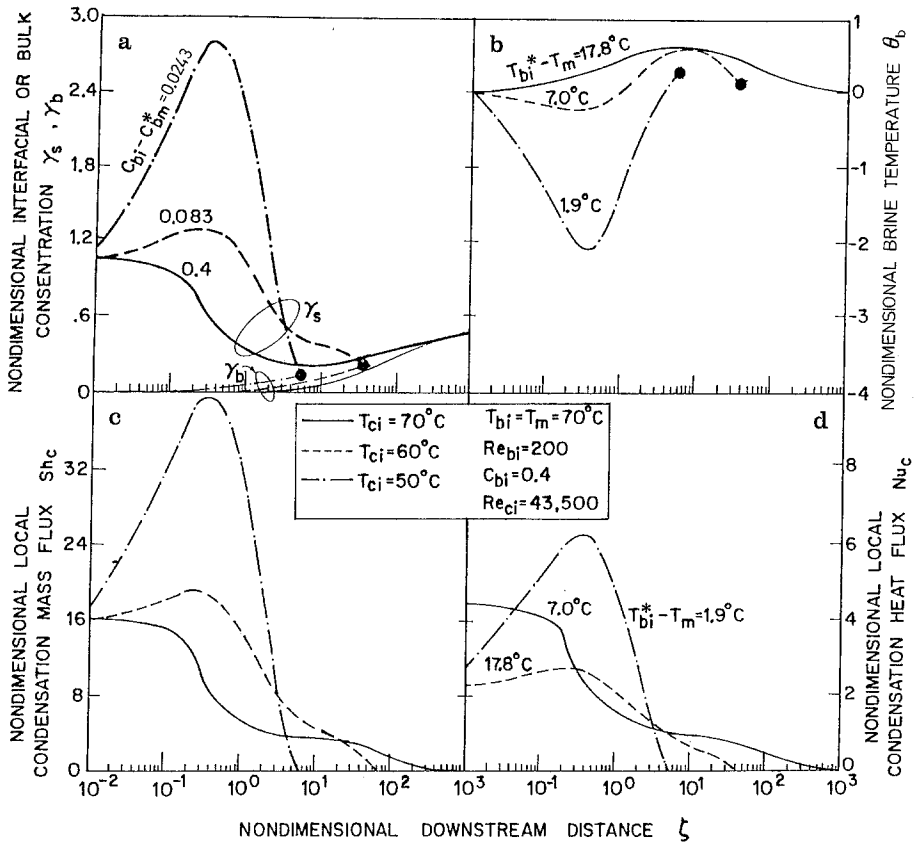

Fig. 8. Various process characteristics along the plate. Effect of vapor temperature level

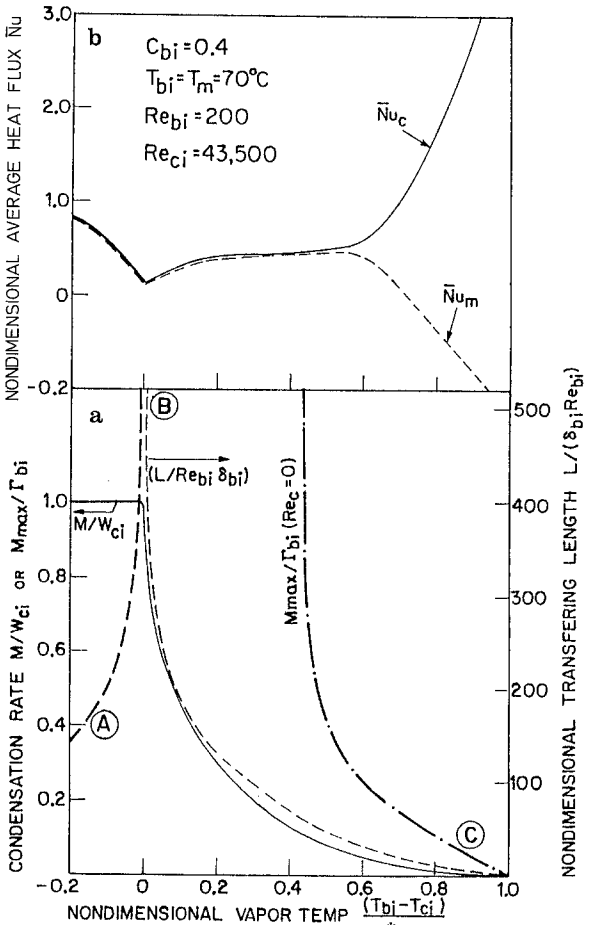

5 Summary and conclusions

A physical model is presented for the analysis of the combined heat and mass transfer process involved in a hygroscopic condensation of vapor over a falling film of a concentrated salt solution. The mass and energy balances over the brine film and vapor phase account for the variation of the physical properties, local flow rate, pressure drop and interfacial heat transfer during the process. These enable evaluation of the process performance under a variety of operating conditions: brine and vapor feed Reynolds numbers, brine concentration and temperature, vapor pressure and temperature and wall temperature. The results yield the concentration temperature and pressure variation along the transfer surface, the corresponding local and average mass and heat fluxes involved in the process, as well as the maximum brine absorption potential and the required transfer length under the specified operating conditions. The main conclusions are:

a) The coupling between the momentum heat and mass transfer process stems mainly from the interdependent driving forces, namely the concentration and temperature differences.

Fig. 9. Effect of vapor temperature level on the overall absorption and heat transfer rates

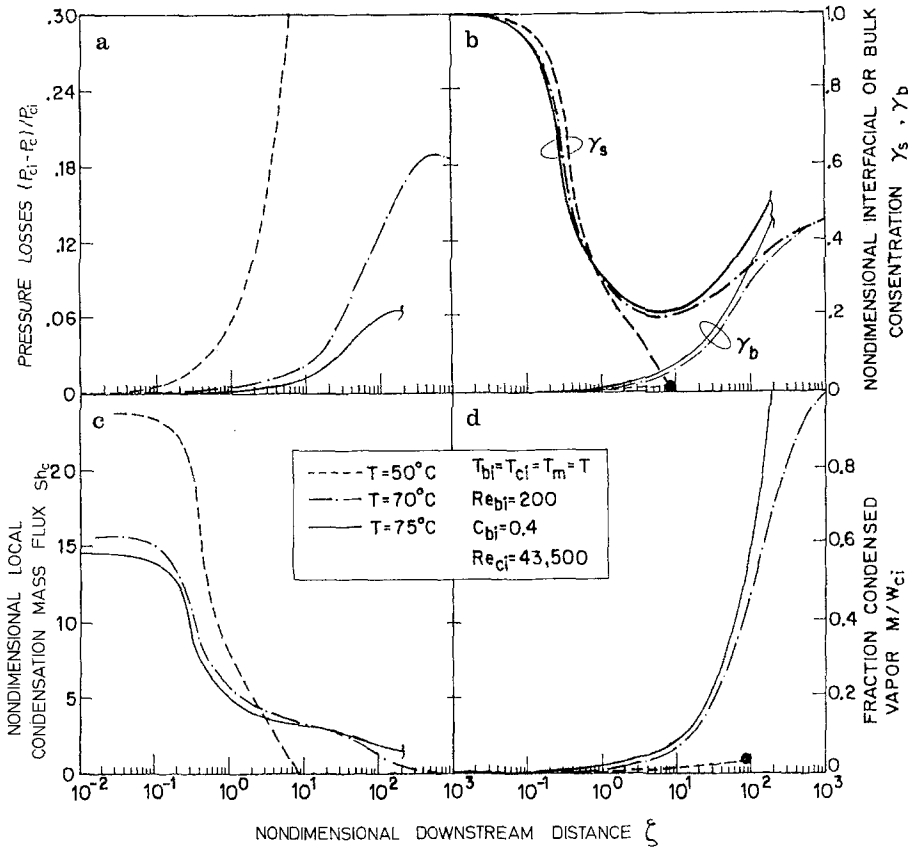

Fig. 10. Effect of process temperature level on the various transfer characteristics along the plate

b) Pressure losses in the vapor phase deteriorate the maximum brine absorption potential and the effective transfer length.

c) The process performance is improved by increasing the brine Reynolds number, increasing the process temperature level, increasing the pressure (and the corresponding saturation temperature) of the vapor, reducing the wall temperature and reducing the Reynolds number of the condensing vapor (high plate spacing).

Appendix A

The conservation equations

1 Mass balances

The differential mass balances over the brine film and vapor phase reads:

$$m=\frac{d\Gamma_b}{dz}=\frac{-dW_c}{dz} \tag{A.1}$$

where Γ_b, W_c are the local brine and vapor mass flow rate per unit width. The local rate of absorption per unit area, m, is related to the local mass transfer coefficient, K_b, by the equation:

$$m=\varrho_b K_b (C_w^*-C_w)=\varrho_b K_b (C_b-C_b^*) \tag{A.2}$$

where $C_w^*=1-C_b^*$ and $C_w=1-C_b$ are the interfacial and bulk concentrations of water in the brine, respectively, and ϱ_b is the brine density. A differential mass balance for the water absorbed in the brine film yields:

$$m\,dz=d[\Gamma_b(1-C_b^*)]=\varrho_b K_b (C_b-C_b^*)\,dz\,. \tag{A.3}$$

Note that the rate of salt flow in the absorbing film is constant, i.e., $\Gamma_b C_B=\Gamma_{bi} C_{bi}=\Gamma_{bo} C_{bo}$ and, by differentiation

$$C_b\frac{d\Gamma_b}{dz}=-\Gamma_b\frac{dC_b}{dz}\,. \tag{A.4}$$

Combining with Eq. (A.3) yields

$$\frac{d\Gamma_b}{dz}=-\frac{\Gamma_{bi} C_{bi}}{C_b^2}\frac{dC_b}{dz}\,. \tag{A.5}$$

The overall condensation rate $M(=\Gamma_{bo}-\Gamma_{bi})$ over a plate length L is related to the dilution rate of the brine solution by

$$\Gamma_{bi} C_{bi}=\Gamma_{bo} C_{bo}=(\Gamma_{bi}+M)\,C_{bo} \tag{A.6}$$

or:

$$M=\int_0^L m\,dL=\Gamma_{bi}\frac{C_{bi}-C_{bo}}{C_{bo}}\,. \tag{A.7}$$

Note that the maximum dilution due to water absorption is obtained as the outlet brine concentration C_{bo} approaches the thermodynamic equilibrium salt concentration at the outlet conditions, i.e.:

$$(C_{bo})_{\min}=C_{bo}^*=C_b^*(P_{co},T_{bo})\,. \tag{A.8}$$

Clearly, this value can be approached only on sufficiently long transfer surfaces.

2 The energy balances

The hygroscopic condensation over the brine initiates a simultaneous heat transfer process. A differential energy balance over the brine film reads:

$$\frac{d(\Gamma_b j_b)}{dz} = -(q_m + q_s) + m j_c \tag{A.9}$$

where j_b and j_c are the respective enthalpies of the liquid solution and vapor phase; q_m and q_s are the heat fluxes from the film to the wall and to the adjacent vapor phase, respectively. Equation (A.9) is simplified by recognizing that $j_b = j_b(C_b, T_b)$, and that

$$\frac{\partial j_b}{\partial T_b} = c_{pb} \tag{A.10}$$

where c_{pb} is the specific heat of the brine. Introducing Eqs. (A.1), (A.4) and (A.10) into (A.9) yields:

$$\Gamma_b c_{pb} \frac{dT_b}{dz} = -q_m - q_s + m\left[j_c - j_b - C_b \frac{\partial j_b}{\partial C_b}\right]$$
$$= -q_m - q_s + m\lambda_{ef}^* \tag{A.11}$$

λ_{ef}^* denotes the effective latent heat of condensation over the brine film. The latter is given by [3]:

$$\lambda_{ef}^* = \lambda^* - c_{pc}(T_b - T_c) - (1-\chi)\lambda \tag{A.12}$$

where λ^* is the heat required to evaporate (or condense) a unit mass of water from a solution of a given concentration, which is in the thermodynamic equilibrium with its superheated vapor at a temperature T_b. λ^* is the latent heat corrected for the sensitive heat loss due to condensation of relatively cold or hot vapor at a temperature $T_c \neq T_b$. $(1-\chi)\lambda$ represents the latent heat loss due to condensation of vapor of quality χ. λ is the latent heat of condensation of pure water.

λ^* may also be obtained from the heat of dilution ΔH_{dil} defined as the heat released (positive) when a solution of given concentration and temperature is diluted with a unit mass of pure water. Since

$$\lambda^* = \lambda + \Delta H_{dil}. \tag{A.13}$$

Substituting Eq. (A.13) into Eq. (A.12) yields:

$$\lambda_{ef}^* = \chi\lambda^* + (1-\chi)\Delta H_{dil} - c_{pc}(T_b - T_c)$$
$$= \chi\lambda + \Delta H_{dil} - c_{pc}(T_b - T_c). \tag{A.14}$$

The local temperature of the adjacent absorbed vapor is derived from a differential energy balance over the vapor phase, which reads:

$$\frac{d[W_c j_c]}{dz} = q_s - m j_c. \tag{A.15}$$

Substituting Eq. (A.1) and $\frac{\partial j_c}{\partial T_c} = c_{pc}$ yields:

$$W_c c_{pc} \frac{dT_c}{dz} = q_s - W_c \frac{\partial j_c}{\partial P_c}\frac{dP_c}{dz}. \tag{A.16}$$

The second term in the RHS of Eq. (A.16) may be neglected when the pressure gradients are low.

3 Momentum balance

A momentum balance on the condensing vapor phase yields the local pressure drop in the condensation compartment:

$$\frac{dP_c}{dz} = -\frac{2\tau_s - 2m u_c}{(d_c - 2\delta_b)} \tag{A.17}$$

where τ_s is the local vapor phase interfacial shear stress, δ_b is the local brine film thickness, and u_c is the local vapor velocity.

Appendix B

The transport coefficients

1 The mass transfer coefficient

The absorption mass transfer coefficient K_b is taken from studies of liquid phase controlled mass transfer into a falling film. However, due to the complicated nature of the wavy free interface, no uniformly accepted method for the prediction of mass transfer coefficients is available. The high Schmidt number of liquids implies that the major mass transfer resistance is located near the gas-liquid interface, and an accurate knowledge of the eddy diffusivity for mass in this region is important. As pointed out by Henstock and Hanratty [5], it is impossible to distinguish, from available measurements, whether waves or turbulence are the controlling factors for the mass transfer, particularly since little is known about the damped region of turbulence close to the interface. Also, the effects of interfacial waviness is not quantitatively clear.

Experimental data of gas absorption into wavy and turbulent falling liquid films are correlated over a wide range of Reynolds and Schmidt numbers by [5, 10, 21]:

$$\tilde{K}_b = \frac{K_b}{D}\left(\frac{\mu_b^2}{\varrho_b^2 g}\right)^{1/3} = \alpha \cdot Re^b\, Sc^{1/2}. \tag{B.1}$$

The correlations suggested by Yih and Chen [21] are adopted here:

$$\tilde{K}_b = 1.099 \times 10^{-2}\, Re_b^{0.3955}\, Sc_b^{1/2}; \quad 49 < Re < 300 \tag{B.2}$$

$$\tilde{K}_b = 2.995 \times 10^{-2}\, Re_b^{0.2134}\, Sc_b^{1/2}; \quad 300 < Re < 1600 \tag{B.3}$$

$$\tilde{K}_b = 9.7777 \times 10^{-4}\, Re_b^{0.6804}\, Sc_b^{1/2}; \quad 1600 < Re < 10{,}500. \tag{B.4}$$

2 The heat transfer coefficient

The heat fluxes to the wall q_m and the adjacent gas stream q_s are related to the corresponding local heat transfer coefficients h_m and h_s and to the temperature driving forces by:

$$q_m = h_m(T_b - T_m) \tag{B.5}$$

$$q_s = h_s(T_b - T_c) \tag{B.6}$$

h_m is evaluated in the smooth laminar region from the well-known Nusselt's solution:

$$h_m = h_{Nu} = \frac{k_b}{\delta_b} = k_b\left(\frac{3}{4}\frac{\mu_b^2}{\varrho_b^2}\frac{Re_b}{g}\right)^{-1/3}. \tag{B.7}$$

In the laminar-wavy region, Kutadeladze [22] correction due to waves amplification is adopted, whereby:

$$h_m = F \cdot h_N; \quad F = 0.8975\, Re_b^{0.11} \tag{B.8}$$

or:

$$h_m = 0.606\, k_b\left(\frac{\mu_b^2}{\varrho_b^2 g}\right)^{-1/3}\left(\frac{Re_b}{4}\right)^{-0.22};$$
$$2.44\left(\frac{\mu_b^4 g}{\varrho_b \sigma_b^3}\right)^{-1/11} \leqq Re_b \leqq 5800\, Pr_b^{-1.06} \tag{B.9}$$

where

$$Pr_b = \frac{c_{pb}\mu_b}{k_b} \tag{B.10}$$

and σ_b is the brine surface tension. In the turbulent region, the Chun and Seban [23] correlation is utilized, whereby:

$$h_m = 6.61 \times 10^{-3}\, k_b \left(\frac{\mu_b^2}{\beta_b^2 g}\right)^{-1/3} Pr_b^{0.65} \left(\frac{Re_b}{4}\right)^{0.4}; \qquad Re_b > 5800\, Pr_b^{-1.06}. \tag{B.11}$$

In the case of an adiabatic wall $h_m \equiv 0$.

The interfacial heat transfer coefficient, h_s, is evaluated by utilizing Groothuis and Hendal [24] correlation for the average interfacial Nusselt number:

$$\overline{Nu_s} = \frac{h_s D_H}{k_b} = 0.029\,(Re_b + Re_c)^{0.87}\, Pr_b^{1/2}\,(\mu_b/\mu_w)^{0.14} \tag{B.12}$$

$D_H = 2d_c$ is the hydraulic radius of the condensation compartment, and Re_c is the local Reynolds number of the condensing vapor phase. At low vapor rates this correlation approaches that of a single phase, and the liquid Reynolds number Re_b predominates. At higher vapor rates, Re_c predominates.

3 The interfacial shear

The pressure losses in the vapor phase resulting from a flow over a wavy film interface are estimated by utilizing Wallis correlation [25] for the interfacial friction factor, f_s:

$$f_s = 0.005\left(1 + 300\,\frac{\delta_b}{D_H}\right) = \frac{\tau_s}{1/2\,\varrho_c u_c^2} \tag{B.13}$$

where ϱ_c is the vapor density.

The local brine film thickness, δ_b, in the laminar region is obtained from the Nusselt's solution:

$$\delta_b = \left[\frac{3}{4}\left(\frac{\mu_b}{\varrho_b}\right)^2 \frac{Re_b}{g}\right]^{1/3} \qquad Re_b \leqq 1600 \tag{B.14}$$

and from Feind [26] correlation in the turbulent region:

$$\delta_b = 0.369\left(\frac{3\,\mu_b^2}{\varrho_b^2 g}\right)^{1/3}\left(\frac{Re_b}{4}\right)^{0.5} \qquad Re_b > 1600\,. \tag{B.15}$$

It is to be noted that the film thickness is used in the present analysis only for estimating the interfacial shear stress via Eq. (B.13). For the relatively low pressure drop associated with condensers, the approximate evaluation of the film thickness by Eqs. (B.14) and (B.15) is rather sufficient.

Note that the entry length, required for the development of the velocity temperature and concentration profiles, is assumed to be small in relation to the active plate length and the transfer coefficients are used for the entire plate length.

References

1. Moalem-Maron, D.; Sideman, S.: Theoretical analysis of a horizontal condenser-evaporator tube. Int. J. Heat Mass Transfer 19 (1976) 259–270
2. Moalem-Maron, D.; Sideman, S.: Theoretical analysis of a horizontal condenser elliptical tube. Trans. ASME J. of Heat Transfer 97 (1975) 352–359
3. Moalem-Maron D.; Brauner, M.: Analysis of power cycle based on absorption condenser evaporator. Report 1. Project 0251. School of Engineering, Tel-Aviv University, submitted to ORMAT Turbines, Ltd. (1983)
4. Brauner, N.; Moalem-Maron, D.; Harel, Z.: Wettability, rewettability and breakdown of thin film of aqueous salt solutions. Desalination 52 (1985) 295–307
5. Henstock, W. H.; Hanratty, T. J.: Gas absorption by a liquid layer flowing on the wall of a pipe. AIChE J. 25 (1979) 122–131
6. Bakopoulos, A.: Liquid-side controlled mass transfer in wetted-wall tubes. German Chem. Eng. 3 (1980) 241–252
7. Chung, D. K.; Mills, A. F.: Experimental study of gas absorption into turbulent falling films of water and ethylene glycol-water mixtures. Int. J. Heat Mass Transfer 19 (1976) 51–59
8. McCready, M. J.; Hanratty, T. J.: Concentration fluctuations close to a gas-liquid interface. AIChE J. 30(5) (1984) 816–817
9. King, C. J.: Turbulent liquid phase mass transfer at a free gas-liquid interface. I/EC Fundamentals 5 (1966) 1–8
10. Bin, A. K.: Mass transfer into turbulent liquid film. Int. J. Heat Mass Transfer 26 (1983) 981–991
11. Kastwia, G.; Stepanek, J. B.: Two phase flow-IV. Gas and liquid side mass transfer coefficients. Chem. Eng. Sci. 29 (1974) 1849
12. McCready, M. J.; Hanratty, T. J.: Gas effect of air shear on gas absorption by liquid film. Private communication (1985)
13. Brumfield, L. K.; Houze, R. N.; Theofanous, T. G.: Turbulent mass transfer at free, gas-liquid interfaces, with applications to film flows. Int. J. Heat Mass Transfer 18 (1975) 1077–1081
14. Brauner, N.; Moalem-Maron, D.: Characteristics of inclined thin films, waviness and the associated mass transfer. Int. J. Heat Mass Transfer 25 (1982) 99–110
15. Brauner, N.; Moalem-Maron, D.: Mass transfer in inclined thin films with intermittent feed. Chem. Eng. J. 28 (1984) 139–150
16. Brauner, N.; Moalem-Maron, D.: Modelling of wavy flow in inclined thin films. Chem. Eng. Sci. 38 (1983) 775–788
17. Yih, S. M.; Seagrave, R. C.: Mass transfer in laminar falling liquid films with accompanying heat transfer and interfacial shear. Int. J. Heat Mass Transfer 23 (1980) 749–758
18. Grigor'eva, N. I.; Nakoryakov, V. E.: Exact solution of combined heat and mass transfer problem during film absorption. Inzh.-fiz. zh. 33 (1977) 983–989
19. Nakoryakov, V. E.; Grigor'eva, N. I.: Calculation of heat and mass transfer in non-isothermal absorption in the entrance region of a falling film. Osn. Khim. Tekhnol. 14 (1980) 483–488
20. Grossman, G.: Heat and mass transfer in film absorption. Handbook of Heat and Mass Transfer. Gulf Publishing, pp. 211–257, 1986
21. Yih, S. M.; Chen, K. Y.: Gas absorption into wavy and turbulent falling liquid films in a wetted wall column. Chem. Eng. Commun. 17 (1982) 123–136
22. Kutadeladze, S. S.: Fundamentals of heat transfer. London: Edward Arnold 1963
23. Chun, K. R.; Seban, R. A.: Heat transfer to evaporating liquid films. J. of Heat Transfer., Trans. ASME, Series C, 93(4) (1971) 391
24. Groothuis, G.; Hendal, W. P.: Heat transfer in two phase flow. Chem. Eng. Sci. 11 (1959) 212–220
25. Wallis, G. B.: One dimensional two phase flow. New York: McGraw-Hill 1969
26. Feind, K.: Stromungsuntersuchungen bei gegenstrom van rieselfilmen und gas lotrechten rohresn. VDI-Forschungsheft, 481 (1960)
27. Brauner, N.; Moalem-Maron, D.; Sideman, S.: Simultaneous mass and heat transfer in direct contact hygroscopic condensation. Proc. 8th Int. Heat Transfer Conf. San Francisco: Tien, C. L.; Carey, V. P.; Ferrell, J. K. (Eds.). New York: 1986, Hemisphere, Vol. 4, pp. 1647–1652

N. Brauner, D. Moalem Maron, and S. Sideman
Dept. of Fluid Mechanics and Heat Transfer University of Tel-Aviv
and Dept. of Chemical Engineering
Technion I.I.T.
Haifa, Israel

Received October 27, 1986